



Interstitial magnetic thermotherapy dosimetry based on shear wave magnetomotive optical coherence elastography

PIN-CHIEH HUANG,^{1,2} ERIC J. CHANEY,¹ RISHYASHRING R. IYER,^{1,3}
DAROLD R. SPILLMAN JR.,¹ BORIS ODINTSOV,¹ NAHIL A. SOBH,¹ AND
STEPHEN A. BOPPART^{1,2,3,4,*}

¹Beckman Institute for Advanced Science and Technology, University of Illinois at Urbana-Champaign, 405 N Mathews Ave, Urbana, IL 61801, USA

²Department of Bioengineering, University of Illinois at Urbana-Champaign, 1406 W Green St, Urbana, IL 61801, USA

³Department of Electrical and Computer Engineering, University of Illinois at Urbana-Champaign, 306 N Wright St, Urbana, IL 61801, USA

⁴Carle-Illinois College of Medicine, University of Illinois at Urbana-Champaign, 807 S Wright St, Champaign, Illinois 61820, USA

*boppart@illinois.edu

Abstract: While magnetic thermoseeds are often utilized in interstitial magnetic thermotherapy (iMT) to enable localized tumor ablation, we propose to extend their use as the perturbative source in magnetomotive optical coherence elastography (MM-OCE) so that the heat-induced elasticity alterations can be ‘theranostically’ probed. MM-OCE measurements were found to agree with indentation results. Tissue stiffening was visualized on iMT-treated porcine liver and canine soft tissue sarcoma specimens, where histology confirmed thermal damages. Additionally, the elasticity was found to increase exponentially and linearly with the conventional thermal dosage metrics and the deposited thermal energy, respectively. Collectively, a physiologically-meaningful, MM-OCE-based iMT dosimetry is feasible.

© 2019 Optical Society of America under the terms of the [OSA Open Access Publishing Agreement](#)

1. Introduction

Magnetic thermotherapy is an emerging cancer treatment that can be performed alone or as an adjuvant to chemotherapy and/or radiotherapy. Magnetic thermotherapy utilizes a high frequency (50 kHz – 15 MHz) alternating magnetic field (AMF) to induce thermal damage to tumor tissues [1]. Among various types of magnetically-induced thermotherapy, interstitial magnetic thermotherapy (iMT) offers an opportunity to deliver rapid, localized, and targeted treatment at tumor sites while reducing potential collateral damage to the surrounding healthy tissues [2–7]. During iMT treatment, a ferromagnetic alloy is implanted at the targeted tissue site, where eddy current can be induced by a rapidly oscillating AMF. The concept of implantation for iMT is similar to that of brachytherapy, where radiation treatment is delivered to the tumor site by placing a small radioactive seed near the tumor. In fact, a thermobrachytherapy seed allowing for both iMT and brachytherapy has been proposed previously [7]. The heating mechanism of iMT is similar to that of clinically available radiofrequency ablation (RFA), which is often performed on hepatic, cerebral, cardiological, and bony abnormalities [8]. During RFA, an RF generator is directly connected to a partially insulated RF electrode, which is inserted into the tissue site of interest; with a conductive grounding pad attached to the body. The generated RF voltage causes a rapidly oscillating current to flow through the human body to induce Joule heating [8]. Compared to brachytherapy, iMT does not require radioactive protection for the surgeons during the implantation of magnetic thermoseeds, as no radioactivity is involved [6]. Compared to RFA

systems, iMT has the advantage of inducing heat remotely and wirelessly. Clinical trials of iMT for oncology have previously been performed on prostate and oral cancers [3–5].

In any kind of cancer treatment, the goal is to provide the maximum amount of damage to the malignant tissues while sparing or minimizing the collateral injury to the surrounding healthy tissues. Often, the maximum therapeutic dose that is allowed is limited by the damage to the healthy tissues [9]. Therefore, an accurate evaluation of the thermal dosage is important. Traditionally, the thermal dosage applied to the tissue has often been estimated via the cumulative equivalent minutes at 43 °C (CEM43). This metric converts different temperature-time history during thermotherapy to a biological isoeffect at 43 °C, an empirically determined “break” point where the survival rates of various cell lines transition from one constant to another [10,11]. However, CEM43 does not fully account for factors such as the thermotolerance effect (which can be an intrinsic biological property, or developed by step-down heating, multiple dose delivery, or exposure to radiation) and the influence of high-temperatures (> 47 °C) that are often seen in ablation [10]. In addition, the assessment of the cross-sectional temperature profile is often challenging [12].

Interestingly, biomechanical properties, such as the viscoelasticity of the tissues, can also be altered because protein denaturation and coagulation can be induced along with temperature elevation [12–15]. This suggests that biomechanical properties could be an alternative physiologically-meaningful indicator of the thermal dosage applied in thermotherapy. Elastography is a technique that probes and/or maps the mechanical characteristics of the tissue with biomedical imaging modalities such as ultrasound, magnetic resonance imaging (MRI), or optical coherence tomography (OCT). Among these clinically available imaging modalities, the finest cross-sectional structural details (μm -scale) and axial displacement sensitivity (nm-scale) are provided by OCT [16–19]. Tissue elasticity can be described by the longitudinal stress-to-strain ratio, or the Young’s modulus, meaning that the stiffness of the sample can be inferred by exerting a certain force and measuring the induced displacement. In optical coherence elastography (OCE), subtle tissue displacements are commonly probed by phase-sensitive OCT, and further spatial and/or temporal analysis of the displacements can allow for elasticity measurements (through quasi-static and/or dynamic OCE) [17].

Magnetomotive optical coherence elastography (MM-OCE) is a branch of dynamic OCE that vibrates tissue with an oscillating magnetic force and probes the temporal tissue displacements for further mechanical assessment [20–25]. Magnetic nanoparticles (MNPs), acting as internal mechanical perturbative sources, can be delivered to the tissues uniformly and induce motions when exposed to an external magnetic field gradient. Subsequently, either the natural or resonant frequency can be extracted from the induced “magnetomotion” and be utilized to infer the elasticity of the homogeneous or heterogeneous tissues [20–24]. In addition, by confining the MNPs to a small cylindrical region at high concentration, a more localized magnetic force can be exerted to induce shear waves, where the wave propagation velocity can be utilized for stiffness quantification [25]. However, the distribution of MNPs in tissues is often hard to control, let alone confining the MNPs into a cylindrical region. Moreover, localized magnetic force was less achievable with the large dimensions of a formed MNP mold ($\varnothing \sim 3 \text{ mm}$) [25]. In contrast, readily accessible magnetic thermoseeds for iMT have well-defined geometries (typically rod-shaped) and are directly inserted at the tumor site. The small dimensions of thermoseeds ($\varnothing \sim 1 \text{ mm}$ [2,4–6]) can also allow for a highly localized mechanical excitation. Therefore, we aim to examine the feasibility of performing shear wave MM-OCE with a rod-shaped magnetic thermoseed serving as an internal, localized perturbative source. Subsequently, the capability of monitoring iMT-induced stiffness changes is further investigated on both normal porcine liver and cancerous soft tissue sarcoma (STS) specimens. Clinically, hepatic tumors are one of the most common diseases amenable for curative ablation treatments [26] and thermotherapy has been reported to improve treatment outcomes for STS [27].

Using a single platform for both therapeutic and diagnostic applications allows for theranostic function. For elastography-based thermotherapy monitoring applications, ultrasound elastography (UE) has been coupled with high-intensity focused ultrasound to assess the alteration of tissue stiffness after treatment on excised chicken breast [28] and *in vivo* human prostate tumors [29]. Additionally, RFA probes have been utilized to both ablate liver tissues and serve as a compressor to allow for ultrasound strain imaging [30]. A mechanical actuator can also be attached to an RFA electrode or microwave antenna to induce shear waves for mapping the elasticity of the treated tissue [31]. Using OCE, our group has previously proposed and demonstrated the use of MNPs for both magnetic fluid hyperthermia and MM-OCE, where a significant shift in resonant frequency was observed in the mechanical spectrum of the treated tissue specimen, qualitatively indicating tissue stiffening [24]. Here, the theranostic function is implemented with a thin embedded magnetic rod, which can be utilized in both iMT as a highly localized heating source (therapeutic), and in shear wave MM-OCE as an internal vibrating source for quantitative elastic measurements (dosimetric/diagnostic).

2. Materials and methods

2.1 Sample preparation and histology

Tissue-mimicking phantoms with different elasticity were prepared by mixing polydimethylsiloxane (PDMS (Clearco Products, Pennsylvania)) with curing agents RTVA and RTVB (Momentive, New York) with a mass ratio of PDMS:RTVA:RTVB ranging from 30:10:1 to 100:10:1 (stiff to soft). Subsequently, 1 mg/g of titanium dioxide (TiO_2) was added to the PDMS solution as scatterers for OCT contrast prior to sonication (>1 hr). Afterward, the sonicated PDMS solution was poured into a Petri dish and heated for >6 hr at 80 °C. Finally, homogeneous PDMS phantoms ($\text{\O} \sim 34$ mm, thickness ~ 8 mm) of various stiffness were produced. To simulate an ablated tissue, a heterogenous phantom was also created (a stiff cylindrical inclusion at the center surrounded by soft medium). A stiff PDMS (PDMS:RTVA:RTVB 30:10:1) was first made, trimmed into a thin cylinder ($\text{\O} \sim 7$ mm), and placed at the center of a Petri dish. Subsequently, the surrounding area was filled with a soft PDMS solution (PDMS:RTVA:RTVB 100:10:1) to create a soft environment. The phantom was heated again for another >6 hr. All phantoms were separated from the Petri dish wall before imaging to minimize boundary effects.

Ex vivo porcine liver tissues were trimmed to rectangular cuboid shapes with dimensions (length \times width \times height) of $\sim 28 \times 28 \times 8$ mm³. In addition, one specimen of excised canine soft tissue sarcoma with dimensions (length \times width \times height) of $\sim 17 \times 9 \times 4$ mm³ was also utilized. For both PDMS phantoms and biological tissues, a ~ 1 cm long carbon steel wire (Malin, Ohio) was inserted in depth at the center to serve as both the magnetic thermoseed for iMT and the vibration source for MM-OCE. The steel wire has a diameter of ~ 220 μm , which is less than that of a 25-gauge syringe (~ 510 μm), radioactive seed (~ 500 – 800 μm [32]), and RFA probe (~ 1.5 mm [31]).

After imaging, the tissues were fixed in neutral-buffered formalin for >6 hr before histological processing. The tissues were embedded in paraffin, sectioned at 5 μm using a microtome (Leica Microsystems, Germany), and stained with Masson Trichrome (Sigma-Aldrich, Missouri) for collagen visualization.

2.2 iMT system setup

The iMT system was built by integrating a pulse generator, heat inductor, water chiller, and a magnetic coil (inner $\text{\O} \sim 3$ cm, 13 turns over 10 cm length) on a portable cart (Fig. 1(c)). The tissue specimen was placed within the coil, where the long-axis of the magnetic thermoseed (rod) was situated in parallel to the induced magnetic field (Fig. 1(b), 1(d)). To heat the porcine liver specimens, the magnetic field strength ranged from 18.1 – 36.0 kA/m

(and 0 kA/m for control), oscillated at 64.7 kHz for 4 min during one iMT treatment. In addition, a canine soft tissue sarcoma (STS) specimen underwent two iMT treatments, both with a magnetic field strength of 25.9 kA/m. The first and second iMT were administered for 2 and 4 min, respectively.

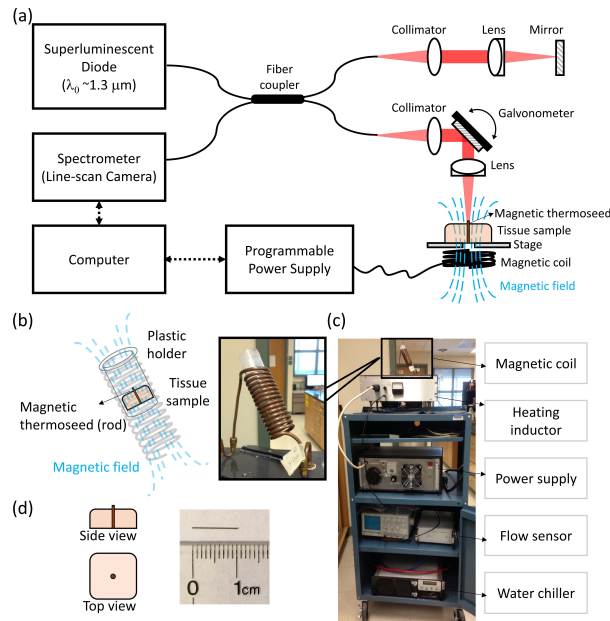


Fig. 1. Schematics and experimental setup of MM-OCE and interstitial magnetic thermotherapy (iMT). (a) Schematics of shear-wave MM-OCE. (b) Illustration of the iMT coil and (c) photograph of the iMT system. (d) (Left) illustration of the placement of the magnetic thermoseed in tissues and (right) photograph of the magnetic thermoseed.

2.3 Temperature monitoring and CEM43 quantification

A thermal camera (FLIR, Oregon) was utilized to monitor the temperature change distributed across the tissue surface during iMT once every minute. Subsequently, the conventional thermal dosage estimation was performed based on the cumulative equivalent minute at 43 °C (CEM43), determined by [10,11]:

$$CEM43 = \sum_{t=0}^{t=t_f} R^{43-\bar{T}} \Delta t, \text{ where } R = \begin{cases} 0.25 & \text{if } \bar{T} < 43^{\circ}\text{C} \\ 0.5 & \text{if } \bar{T} \geq 43^{\circ}\text{C} \end{cases} \quad (1)$$

Here t is the time instant from 0 to t_f , Δt and \bar{T} are the temporal interval (1 min) and the average temperature between two successive time points, respectively, and R is the empirically determined constant related to the cell killing rate. Note that the measurable temperature was limited to the sample surface.

2.4 Shear wave MM-OCE system setup and data acquisition

An OCE system requires a mechanical excitation source to delicately vibrate the tissue, and an OCT imaging system to detect the responding tissue displacements. Here, an alternating magnetic force was exerted on the magnetic thermoseed inserted in the tissue via a customized magnetic solenoid and programmable power supply. The magnetic solenoid

produced a magnetic field with a peak-to-peak strength of ~ 4.09 kA/m at 5 mm away from the sample. To produce a sinusoidal magnetic force, the driving voltage carrying a square root of sine waveform was sent to the power supply. The magnetomotive modulation frequency was kept low (~ 460 Hz) to prevent additional heating during MM-OCE measurement. The chamber containing the coil was continuously perfused with water as a cooling agent during magnetic excitation.

The spectral-domain OCT imaging system consisted of a superluminescent diode (Thorlabs, New Jersey) with a wavelength of $\sim 1325 \pm 50$ nm as a light source, and a spectrometer with an InGaAs line-scan camera (Goodrich, North Carolina) at the detection arm. The axial and lateral resolution were ~ 8 μm and ~ 16 μm , respectively. The displacement sensitivity of the system at the line scan rate utilized (~ 92 kHz) was ~ 3 nm (optical distance). M-B mode data were acquired, where multiple M-scans (over ~ 22 ms for the liver samples and ~ 4 ms for the STS specimen) were collected at different lateral locations. Note that as the STS specimen was comparatively small (detailed in Section 2.1), less magnetomotive modulation cycles were provided to the STS specimen to reduce the excitation energy and hence minimize the boundary effect. The lateral pixel resolution was ~ 11 μm .

2.5 Shear wave MM-OCE data processing

The harmonic stimulating force that originated from the centered magnetic rod (which generated a magnetic field gradient predominantly in the axial direction) induced a cylindrical shear wave that propagated along the radial distance (r) through the sample, and vibrated in the axial direction with a modulated angular frequency (ω) over time (t). The axial displacement can be approximated as $u_z(r) \propto (i/\sqrt{kr})e^{i(kr - \omega t - \frac{\pi}{4})}$ at a sufficiently far distance ($kr > 1$, where k is the shear wave number that can be expressed as $k = \omega/c_s$) [33]. Subsequently, the shear wave velocity (c_s) can be acquired. Based on a Kelvin-Voigt model, Young's modulus (E) can thus be calculated via $E = 2(1 + \nu)\rho c_s^2$ for a linear, elastic, isotropic, and locally homogeneous sample [25] with a certain Poisson ratio ν (~ 0.5 for PDMS and ~ 0.47 for soft tissues [34,35]) and mass density ρ (~ 970 kg/m³ for PDMS and ~ 1040 kg/m³ for soft tissues). Note that although Rayleigh waves could possibly be generated during the magnetic excitation as well, we did not take its effect into account as the difference between Rayleigh and shear wave velocities was as small as 5% [36].

Similar to our previous study [25,37], standard OCT processing (i.e. background subtraction, k-linearization, dispersion correction, and Fourier transform) was performed on each M-scan, where axial displacement was extracted from the phase difference between adjacent M-scans (note that the phase derivative was calculated in the complex form, where median filters were applied to both the real and imaginary parts prior to taking the angles). Afterward, bandpass filtering at the modulated frequency ω was performed on the single-sided Fourier transform spectrum, where the subsequent inverse Fourier transform resulted in a complex analytic sinusoid with a phase lag $\Delta\phi$. By linear fitting the phase delay along time over a certain radial distance Δr (~ 78 μm), the local shear wave velocity could be obtained using $c_s = \omega\Delta r / \Delta\phi$. Shown in Fig. 2 and [Visualization 1](#), softer samples exhibited a greater phase gradient over time, $\Delta\phi / \Delta r$, and slower shear wave propagation. A change in both phase gradient and wave propagation velocity, c_s , was only observed on the mechanically heterogeneous sample. Subsequently, a cross-sectional Young's modulus (E) map could be obtained, where thresholding was performed based on both the intensity and the goodness-of-fit of the phase gradient ($R^2 > 0.8$).

3. Results

3.1 Tissue-mimicking phantoms

OCE maps of both homogeneous and heterogeneous PDMS phantoms are visualized in Fig. 2, where a higher Young's modulus (E) value was observed on phantoms fabricated with a higher curing agent ratio. In addition, obvious mechanical contrast was seen from the heterogeneous sample. The average Young's moduli obtained from the two-dimensional OCE maps for each homogeneous phantom were compared to those from mechanical indentation testing with a spherical indenter ($\varnothing \sim 2.5$ mm), where each value of E was obtained by fitting the force-displacement curve to the Hertzian model. As seen in Fig. 3, the two measurements correlated well with each other (Pearson's $r = 0.965$, $N = 16$) and have an almost one-to-one correspondence (mean difference = 0.558 kPa), suggesting a comparable performance between the two approaches.

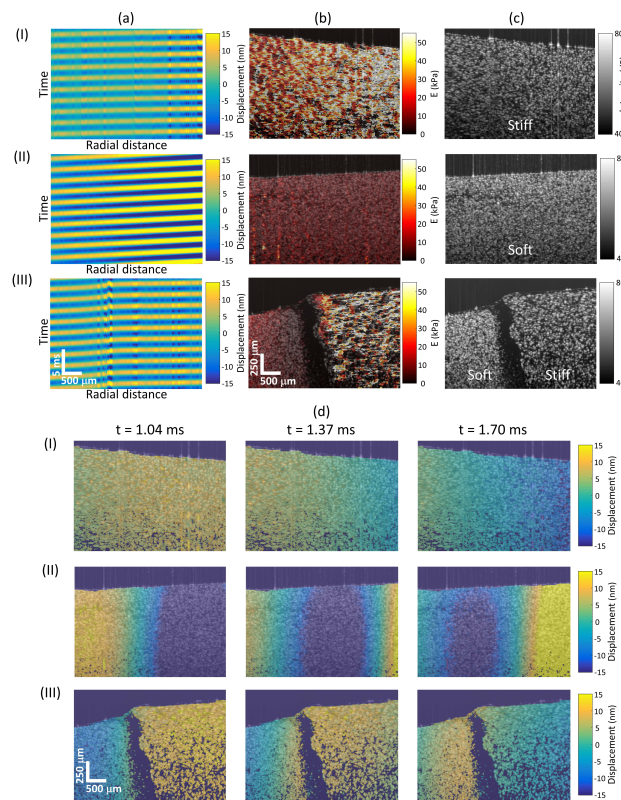


Fig. 2. Representative PDMS phantom results. (a) Space-time plots, (b) reconstructed Young's modulus (E) maps, (c) structural OCT images, and (d) shear wave propagation (full video shown in Visualization 1 at 120 fps) of the (I) uniformly stiff, (II) uniformly soft, and (III) heterogeneous soft-stiff (left-right) samples.

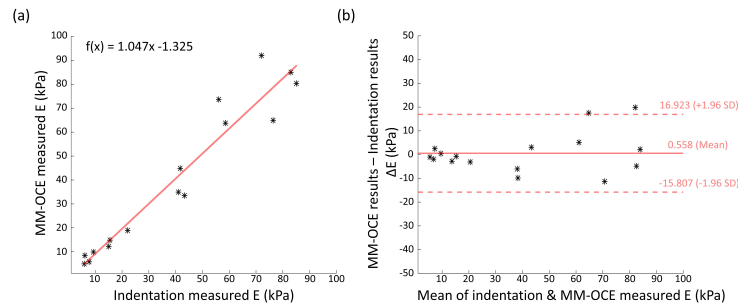


Fig. 3. Comparison between MM-OCE and indentation measurements performed on homogeneous PDMS phantoms. (a) Young's modulus values obtained by both methods showed a good linear correlation (Pearson's $r = 0.965$) and agreement (slope = 1.047, with a negligible offset = -1.325 kPa) with each other. (b) Bland-Altman plot also showed a good agreement between the two measurements (mean difference = 0.558 kPa). Sample size $N = 16$.

3.2 iMT-treated ex vivo porcine liver

Tissue elasticity of iMT-treated porcine liver specimens, before and after therapy, were imaged with the described MM-OCE method, where the magnetic thermoseed served as both the heating and mechanical perturbative source. Both shear wave propagation and the E maps of each liver specimen are visualized, where a significant increase in both the shear wave propagation velocity (c_s) and value of E were only observed from the iMT-treated specimen (Fig. 4(III), 4(V), and Visualization 2), along with an obvious temperature elevation near the thermoseed (Fig. 4(I)). Interestingly, there is a gradual spatial change observed in the stiffness (i.e. higher values of E near the thermoseed) in Fig. 4(III). The corresponding Masson Trichrome-stained histological slices (Fig. 4(IV)) also showed an obvious 'burn mark' at the site near the heat source, where a loss of collagen (absence of blue staining) can be found. In contrast, the control tissue (field strength = 0 kA/m) did not show any changes in the surface temperature, c_s , E map, or histology. Collectively, it is suggested that the spatially varying tissue stiffening was a result of iMT-generated thermal damage.

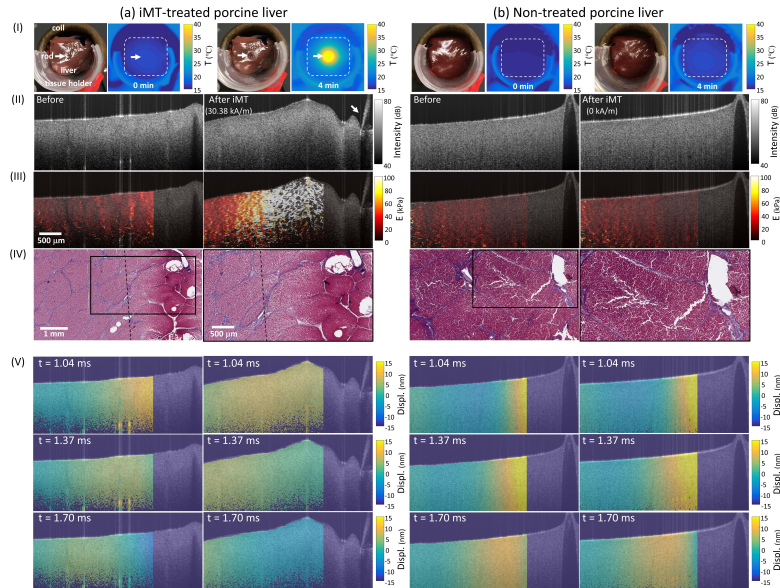


Fig. 4. Representative results of (a) iMT-treated and (b) non-treated porcine liver specimens. (I) Photographs obtained (left) before and (right) after treatment; thermal images acquired at the (left) 0th and (right) 4th min of the treatment. (II) Structural OCT images and (III) reconstructed Young's modulus (E) maps obtained (left) before and (right) after iMT treatment. White arrows in (I) and (II) indicate the locations of the magnetic thermoseed. (IV) (Left) Post-treatment Masson Trichrome-stained histology and (right) a zoomed-in area. Collagen is stained blue. The ablation zone was delineated with the dashed line. (V) Shear wave propagation captured at different temporal instants were also visualized (full video shown in Visualization 2 at 120 fps).

The altered elasticity was quantified by the ' E ratio', which was obtained by normalizing the average Young's modulus after iMT over that before iMT (i.e. $E \text{ ratio} = E_{\text{after iMT}} / E_{\text{before iMT}}$). Comparing this E ratio with the corresponding CEM43 metrics, an exponential correlation (Pearson's $r = 0.799$, $N = 27$) was observed (Fig. 5(a)). Interestingly, a similar correlation was previously reported in the literature, where the shear modulus ratio obtained after water bath heating of rat leg muscle was exponentially associated with CEM43 [15]. In contrast, the ratio of the average OCT intensity after and before iMT has a value close to unity for all data (OCT intensity ratio: 0.98 ± 0.02 , $N = 27$), implying negligible variation between treated and untreated scenarios. Note that the E , CEM43, and OCT intensity values compared here were all averaged over the same area. In addition, our porcine liver results manifested as a sharp increase in the E ratio starting from CEM43 between $8.5 \times 10^{-2} - 4.6 \times 10^2$ min, which was partially comparable to the thermal damage threshold reported in the literature. To date, the lowest CEM43 reported to cause thermal damage in canine livers was 9.9 min, while thermal coagulation was observed on porcine livers at CEM43 = 320 min [38,39]. Tissue necrosis was shown in rabbit and porcine livers at CEM43 between $2 \times 10^5 - 8.6 \times 10^{11}$ min [39], which overlaps with the CEM43 coverage that corresponds to higher E ratios in our data.

To investigate the relationship between the power (P) absorbed by the ferromagnetic thermoseed (rod) from the axially parallel magnetic field and the corresponding elasticity change induced, the values of the E ratio were further compared to the square of the applied field strength ($|H_0|^2$), as this relationship, i.e. $P \propto |H_0|^2$, holds validity given our initial

assumption that the geometrical and electromagnetic properties of the thermoseed remained constant during iMT [40]. The result (Fig. 5(b)) shows that the E ratio is linearly related to $|H_0|^2$ (Pearson's $r = 0.938$, $N = 27$), which physically relates the stiffening to the thermal energy generated.

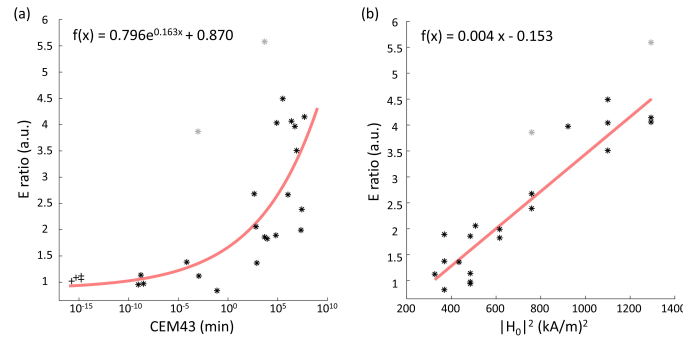


Fig. 5. Correlation between (a) Young's modulus ratio (E ratio) and CEM43 (Pearson's $r = 0.799$), and (b) E ratio and squared magnetic field strength ($|H_0|^2$) (Pearson's $r = 0.938$) in porcine liver specimens. Note that outliers (indicated in gray) were excluded from the fitting and '+' denotes the non-treated tissues. The outliers were defined as the datapoints which deviated from the baseline model by 1.5 standard deviations. Sample size of the non-treated and treated samples were 4 and 23, respectively.

3.3 Ex vivo canine soft tissue sarcoma (STS)

Other than normal tissues, the feasibility of evaluating iMT dosage based on shear wave MM-OCE was also performed on a canine STS specimen. Again, the shear wave propagation (Fig. 6(V) and Visualization 3) and elasticity map (Fig. 6(II)) of the tissue was visualized before and after each iMT treatment. Surface temperature profiles were recorded during iMT (Fig. 6 (III)) and Masson Trichrome staining was performed after the treatments (Fig. 6(IV)).

Similar to the porcine liver, STS tissues stiffened after iMT. Additionally, a monotonic increase in the average E value was observed as more doses were provided. In fact, a higher value of E (18.0, 44.2, and 140.9 kPa for before, after first iMT, and after second iMT treatments, respectively) corresponded to a higher CEM43 value (7.8×10^4 and 3.1×10^9 for the first and second iMT treatments, respectively). Unlike the porcine liver data, a higher mechanical heterogeneity was observed in the treated STS tissues, which potentially reflects the expected heterogeneity of the local anatomy or the thermal sensitivities across the tumor microenvironment. Nevertheless, an increase in local values of E was observed across the tissue. In addition, a generally lower collagen content was present near the heat source, similar to the observation in the liver specimens, suggesting thermal damage.

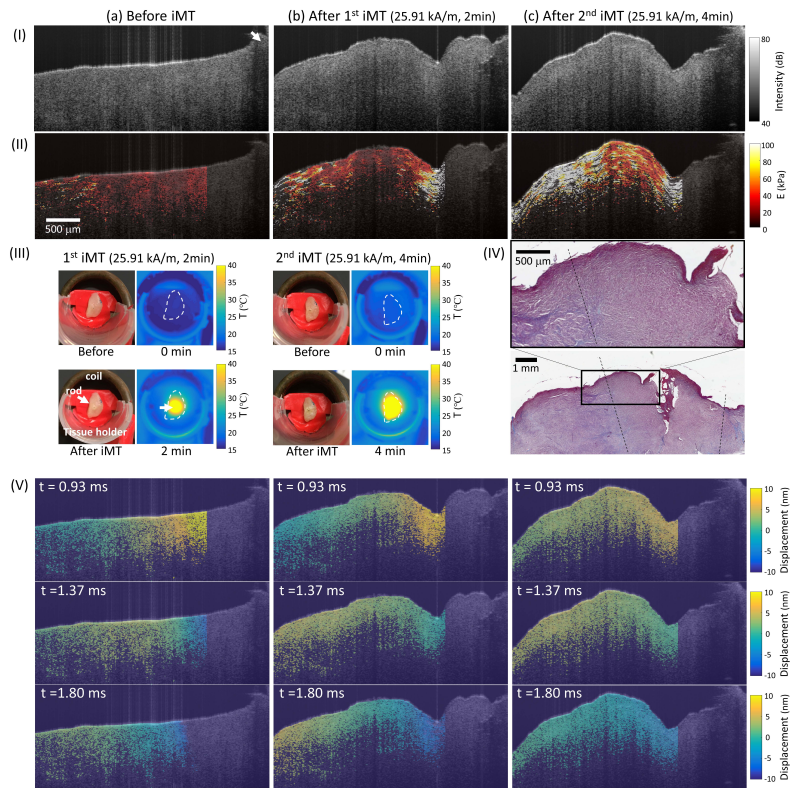


Fig. 6. Representative results of a canine soft tissue sarcoma (STS) specimen (a) before treatment, (b) after 1st iMT, and (c) after 2nd iMT. (I) Structural OCT images and (II) reconstructed Young's modulus (E) maps. (III) Photographs obtained (left) before and (right) after each treatment; thermal images acquired at the (left) 0th and (right) 4th min of each treatment. White arrows in (I) and (III) indicate the locations of the magnetic thermoseed. (IV) (Bottom) Post-treatment Masson Trichrome-stained histology and (top) a zoomed-in area. Collagen is stained blue. The ablation zone was delineated with the dashed line. (V) Shear wave propagation captured at three temporal instants were also visualized (full video shown in Visualization 3 at 120 fps).

4. Conclusions

A magnetic-rod-based shear wave MM-OCE has been successfully developed and utilized to visualize and quantify the iMT-induced thermal damage at the tissue cross-section for both normal liver and soft tissue sarcoma (STS) specimens. Young's modulus (E) quantified with the proposed method correlated well with that from mechanical indentation tests, as demonstrated on PDMS phantoms. On iMT-treated tissue specimens, a significant increase in tissue elasticity was observed while the OCT intensity exhibited negligible changes. Furthermore, Young's modulus maps of the iMT-treated porcine liver and canine STS tissues exhibited patterns similar to their corresponding Masson Trichrome-stained histological sections, where there was an apparent loss of collagen structures (due to thermal coagulation) near the localized heating sites. For the liver specimens, changes in elasticity were found to be exponentially related to the conventional temperature-based thermal damage metrics (CEM43) and linearly proportional to the power absorption of the ferromagnetic thermoseed. Collectively, the results suggest that the elasticity alteration probed by shear wave MM-OCE

could be exploited to serve as a physically and physiologically meaningful thermal dosage metric for iMT.

OCT-based assessment of thermal damage in biological tissues has been widely investigated, where heat-induced alterations can be inferred from tissue morphology, backscattering, and/or birefringence [41–43]. While OCE has previously demonstrated its capability of detecting thermally-altered biomechanical properties and dynamics for cartilages undergoing water-bath heating [44], little has been explored for cancer treatment monitoring on soft tissues. MM-OCE, as demonstrated here, has not only provided an opportunity for elasticity-based thermal dosage evaluation, but has also highlighted the theranostic function of the magnetic thermoseed, which allows for both therapeutic and dosimetric functions. Expanding from this study, it would be interesting to examine the performance of MM-OCE-based iMT dosimetry using a temperature-regulated magnetic thermoseed, where the heating efficiency diminishes above the Curie temperature of the ferromagnetic alloy [4,5]. Changes of the biomechanical tissue properties in the nonlinear elastic regime, or in more anisotropic tissues, can be investigated as well, where the latter is permitted by the inherent rod-shaped geometry of the thermoseed [45]. Additionally, theranostic functions can hypothetically be enabled with OCE in other types of thermotherapy. For instance, laser ablation dosage can potentially be assessed with laser-induced elastic wave characteristics or deformation amplitudes [46,47]; ultrasound-ablated tissues can likely be evaluated with acoustic radiation force OCE [48].

In clinical practice, ultrasound, computed tomography (CT), and MRI are currently utilized to guide the placement of RFA probes and evaluate ablation outcomes [49]. With previously demonstrated intraoperative imaging capabilities [50], an OCT-assisted clinical environment is also foreseen, where handheld or catheter-based OCT can be utilized to both detect the local tumor microstructure and/or image the altered mechanical response of tissue through morphological alteration [50–52]. By incorporating magnetomotive components into a handheld or catheter-based OCT platform, *in situ* MM-OCE-based thermal dosage evaluation may be feasible in the future, serving as a physiologically-meaningful and complementary approach for real-time thermal treatment dosimetry.

Funding

National Institute of Health (NCI, R01CA213149; NIBIB, R01EB013723).

Acknowledgements

P.-C. Huang would like to acknowledge the Government Scholarship to Study Abroad (GSSA) from the Ministry of Education, Taiwan. The authors would like to thank Dr. Christina Cocca (Department of Veterinary Clinical Medicine, University of Illinois at Urbana-Champaign, IL) for providing the excised canine soft tissue sarcoma tissues. The authors would also like to thank Dr. Adeel Ahmad (formerly from the Department of Electrical and Computer Engineering, University of Illinois at Urbana-Champaign, IL) for the helpful discussions at the early stage of this study. Additional information can be found at: <http://biophotonics.illinois.edu>.

Disclosures

The authors declare that there are no conflicts of interest related to this article.

References

1. M. Dewhurst, P. R. Stauffer, S. Das, O. I. Craciunescu, and Z. Vujaskovic, "Hyperthermia," in *Clinical Radiation Oncology*, L. L. Gunderson, and J. E. Tepper, eds. (Elsevier, 2015), pp. 381–398.
2. J. A. Paulus, J. S. Richardson, R. D. Tucker, and J. B. Park, "Evaluation of inductively heated ferromagnetic alloy implants for therapeutic interstitial hyperthermia," *IEEE Trans. Biomed. Eng.* **43**(4), 406–413 (1996).

3. I. Tohnai, Y. Goto, Y. Hayashi, M. Ueda, T. Kobayashi, and M. Matsui, "Preoperative thermochemotherapy of oral cancer using magnetic induction hyperthermia (Implant Heating System: IHS)," *Int. J. Hyperthermia* **12**(1), 37–47 (1996).
4. S. Deger, D. Boehmer, I. Türk, J. Roigas, V. Budach, and S. A. Loening, "Interstitial hyperthermia using self-regulating thermoseeds combined with conformal radiation therapy," *Eur. Urol.* **42**(2), 147–153 (2002).
5. R. D. Tucker, "Use of interstitial temperature self-regulating thermal rods in the treatment of prostate cancer," *J. Endourol.* **17**(8), 601–607 (2003).
6. Q.-S. Xia, X. Liu, B. Xu, T.-D. Zhao, H.-Y. Li, Z.-H. Chen, Q. Xiang, C.-Y. Geng, L. Pan, R.-L. Hu, Y. J. Qi, G. F. Sun, and J. T. Tang, "Feasibility study of high-temperature thermoseed inductive hyperthermia in melanoma treatment," *Oncol. Rep.* **25**(4), 953–962 (2011).
7. G. Warrell, D. Shvydka, and E. I. Parsai, "Use of novel thermobrachytherapy seeds for realistic prostate seed implant treatments," *Med. Phys.* **43**(11), 6033–6048 (2016).
8. S. N. Goldberg, "Radiofrequency tumor ablation: principles and techniques," *Eur. J. Ultrasound* **13**(2), 129–147 (2001).
9. M. Tubiana, "The future of hyperthermia," *Natl. Cancer Inst. Monogr.* **61**, 539–543 (1982).
10. S. A. Sapareto and W. C. Dewey, "Thermal dose determination in cancer therapy," *Int. J. Radiat. Oncol. Biol. Phys.* **10**(6), 787–800 (1984).
11. M. W. Dewhurst, B. L. Vigiante, M. Lora-Michiels, M. Hanson, and P. J. Hoopes, "Basic principles of thermal dosimetry and thermal thresholds for tissue damage from hyperthermia," *Int. J. Hyperthermia* **19**(3), 267–294 (2003).
12. E. Sapin-de Brosse, J. L. Gennisson, M. Pernot, M. Fink, and M. Tanter, "Temperature dependence of the shear modulus of soft tissues assessed by ultrasound," *Phys. Med. Biol.* **55**(6), 1701–1718 (2010).
13. T. Wu, J. P. Felmlee, J. F. Greenleaf, S. J. Riederer, and R. L. Ehman, "Assessment of thermal tissue ablation with MR elastography," *Magn. Reson. Med.* **45**(1), 80–87 (2001).
14. N. Benech and C. A. Negreira, "Monitoring heat-induced changes in soft tissues with 1D transient elastography," *Phys. Med. Biol.* **55**(6), 1753–1765 (2010).
15. E. S. Brosse, M. Pernot, and M. Tanter, "The link between tissue elasticity and thermal dose *in vivo*," *Phys. Med. Biol.* **56**(24), 7755–7765 (2011).
16. B. F. Kennedy, K. M. Kennedy, and D. D. Sampson, "A review of optical coherence elastography: Fundamentals, techniques and prospects," *IEEE J. Sel. Top. Quantum Electron.* **20**(2), 272–288 (2014).
17. X. Liang, V. Crecea, and S. A. Boppart, "Dynamic optical coherence elastography: A review," *J. Innov. Opt. Health Sci.* **3**(4), 221–233 (2010).
18. J. A. Mulligan, G. R. Untracht, S. N. Chandrasekaran, C. N. Brown, and S. G. Adie, "Emerging approaches for high-resolution imaging of tissue biomechanics with optical coherence elastography," *IEEE J. Sel. Top. Quantum Electron.* **22**(3), 246–265 (2016).
19. K. V. Larin and D. D. Sampson, "Optical coherence elastography - OCT at work in tissue biomechanics [Invited]," *Biomed. Opt. Express* **8**(2), 1172–1202 (2017).
20. V. Crecea, A. L. Oldenburg, X. Liang, T. S. Ralston, and S. A. Boppart, "Magnetomotive nanoparticle transducers for optical rheology of viscoelastic materials," *Opt. Express* **17**(25), 23114–23122 (2009).
21. A. L. Oldenburg and S. A. Boppart, "Resonant acoustic spectroscopy of soft tissues using embedded magnetomotive nanotransducers and optical coherence tomography," *Phys. Med. Biol.* **55**(4), 1189–1201 (2010).
22. V. Crecea, A. Ahmad, and S. A. Boppart, "Magnetomotive optical coherence elastography for microrheology of biological tissues," *J. Biomed. Opt.* **18**(12), 121504 (2013).
23. A. Ahmad, P.-C. Huang, N. A. Sobh, P. Pande, J. Kim, and S. A. Boppart, "Mechanical contrast in spectroscopic magnetomotive optical coherence elastography," *Phys. Med. Biol.* **60**(17), 6655–6668 (2015).
24. P.-C. Huang, P. Pande, A. Ahmad, M. Marjanovic, D. R. Spillman, Jr., B. Odintsov, and S. A. Boppart, "Magnetomotive optical coherence elastography for magnetic hyperthermia dosimetry based on dynamic tissue biomechanics," *IEEE J. Sel. Top. Quantum Electron.* **22**(4), 104–119 (2016).
25. A. Ahmad, J. Kim, N. A. Sobh, N. D. Shemonski, and S. A. Boppart, "Magnetomotive optical coherence elastography using magnetic particles to induce mechanical waves," *Biomed. Opt. Express* **5**(7), 2349–2361 (2014).
26. T. W. Kang and H. Rhim, "Recent advances in tumor ablation for hepatocellular carcinoma," *Liver Cancer* **4**(3), 176–187 (2015).
27. L. H. Lindner and R. D. Issels, "Hyperthermia in soft tissue sarcoma," *Curr. Treat. Options Oncol.* **12**(1), 12–20 (2011).
28. R. Iwasaki, R. Takagi, R. Nagaoka, H. Jimbo, S. Yoshizawa, Y. Saijo, and S.-i. Umemura, "Monitoring of high-intensity focused ultrasound treatment by shear wave elastography induced by two-dimensional-array therapeutic transducer," *Jpn. J. Appl. Phys.* **55**(7S1), 07KF05 (2016).
29. R. Souchon, O. Rouvière, A. Gelet, V. Detti, S. Srinivasan, J. Ophir, and J. Y. Chapelon, "Visualisation of HIFU lesions using elastography of the human prostate *in vivo*: preliminary results," *Ultrasound Med. Biol.* **29**(7), 1007–1015 (2003).
30. T. Varghese, J. A. Zagzebski, and F. T. Lee, Jr., "Elastographic imaging of thermal lesions in the liver *in vivo* following radiofrequency ablation: preliminary results," *Ultrasound Med. Biol.* **28**(11-12), 1467–1473 (2002).
31. R. J. Dewall, T. Varghese, and C. L. Brace, "Visualizing *ex vivo* radiofrequency and microwave ablation zones using electrode vibration elastography," *Med. Phys.* **39**(11), 6692–6700 (2012).

32. A. K. Robertson, P. S. Basran, S. D. Thomas, and D. Wells, "CT, MR, and ultrasound image artifacts from prostate brachytherapy seed implants: the impact of seed size," *Med. Phys.* **39**(4), 2061–2068 (2012).
33. M. Orescanin and M. Insana, "Shear modulus estimation with vibrating needle stimulation," *IEEE Trans. Ultrason. Ferroelectr. Freq. Control* **57**(6), 1358–1367 (2010).
34. R. H. Pritchard, P. Lava, D. Debruyne, and E. M. Terentjev, "Precise determination of the Poisson ratio in soft materials with 2D digital image correlation," *Soft Matter* **9**(26), 6037–6045 (2013).
35. C. Li, G. Guan, R. Reif, Z. Huang, and R. K. Wang, "Determining elastic properties of skin by measuring surface waves from an impulse mechanical stimulus using phase-sensitive optical coherence tomography," *J. R. Soc. Interface* **9**(70), 831–841 (2012).
36. F. Zvietcovich, J. P. Rolland, J. Yao, P. Meemon, and K. J. Parker, "Comparative study of shear wave-based elastography techniques in optical coherence tomography," *J. Biomed. Opt.* **22**(3), 35010 (2017).
37. S. G. Adie, X. Liang, B. F. Kennedy, R. John, D. D. Sampson, and S. A. Boppart, "Spectroscopic optical coherence elastography," *Opt. Express* **18**(25), 25519–25534 (2010).
38. G. C. van Rhoon, T. Samaras, P. S. Yarmolenko, M. W. Dewhurst, E. Neufeld, and N. Kuster, "CEM43°C thermal dose thresholds: a potential guide for magnetic resonance radiofrequency exposure levels?" *Eur. Radiol.* **23**(8), 2215–2227 (2013).
39. P. S. Yarmolenko, E. J. Moon, C. Landon, A. Manzoor, D. W. Hochman, B. L. Viglianti, and M. W. Dewhurst, "Thresholds for thermal damage to normal tissues: an update," *Int. J. Hyperthermia* **27**(4), 320–343 (2011).
40. S. A. Haider, T. Cetas, J. Wait, and J.-S. Chen, "Power absorption in ferromagnetic implants from radiofrequency magnetic fields and the problem of optimization," *IEEE Trans. Microw. Theory Tech.* **39**(11), 1817–1827 (1991).
41. S. A. Boppart, J. Herrmann, C. Pitris, D. L. Stamper, M. E. Brezinski, and J. G. Fujimoto, "High-resolution optical coherence tomography-guided laser ablation of surgical tissue," *J. Surg. Res.* **82**(2), 275–284 (1999).
42. C. P. Fleming, K. J. Quan, H. Wang, G. Amit, and A. M. Rollins, "*In vitro* characterization of cardiac radiofrequency ablation lesions using optical coherence tomography," *Opt. Express* **18**(3), 3079–3092 (2010).
43. D. Herranz, J. Lloret, S. Jiménez-Valero, J. L. Rubio-Guivernau, and E. Margallo-Balbás, "Novel catheter enabling simultaneous radiofrequency ablation and optical coherence reflectometry," *Biomed. Opt. Express* **6**(9), 3268–3275 (2015).
44. C.-H. Liu, M. N. Skryabina, J. Li, M. Singh, E. N. Sobol, and K. V. Larin, "Measurement of the temperature dependence of Young's modulus of cartilage by phase-sensitive optical coherence elastography," *Quantum Electron.* **44**(8), 751–756 (2014).
45. J.-L. Gennisson, S. Catheline, S. Chaffai, and M. Fink, "Transient elastography in anisotropic medium: application to the measurement of slow and fast shear wave speeds in muscles," *J. Acoust. Soc. Am.* **114**(1), 536–541 (2003).
46. C. Li, Z. Huang, and R. K. Wang, "Elastic properties of soft tissue-mimicking phantoms assessed by combined use of laser ultrasonics and low coherence interferometry," *Opt. Express* **19**(11), 10153–10163 (2011).
47. N. Leartprapun, R. R. Iyer, G. R. Untracht, J. A. Mulligan, and S. G. Adie, "Photonic force optical coherence elastography for three-dimensional mechanical microscopy," *Nat. Commun.* **9**(1), 2079 (2018).
48. K. Zhou, N. Le, Z. Huang, and C. Li, "High-intensity-focused ultrasound and phase-sensitive optical coherence tomography for high resolution surface acoustic wave elastography," *J. Biophotonics* **11**(2), e201700051 (2018).
49. M. Ahmed, L. Solbiati, C. L. Brace, D. J. Breen, M. R. Callstrom, J. W. Charboneau, M.-H. Chen, B. I. Choi, T. de Baère, G. D. Dodd 3rd, D. E. Dupuy, D. A. Gervais, D. Gianfelice, A. R. Gillams, F. T. Lee, Jr., E. Leen, R. Lencioni, P. J. Littrup, T. Livraghi, D. S. Lu, J. P. McGahan, M. F. Meloni, B. Nikolic, P. L. Pereira, P. Liang, H. Rhim, S. C. Rose, R. Salem, C. T. Sofocleous, S. B. Solomon, M. C. Soulen, M. Tanaka, T. J. Vogl, B. J. Wood, and S. N. Goldberg; International Working Group on Image-Guided Tumor Ablation; Interventional Oncology Sans Frontières Expert Panel; Technology Assessment Committee of the Society of Interventional Radiology; Standard of Practice Committee of the Cardiovascular and Interventional Radiological Society of Europe, "Image-guided tumor ablation: standardization of terminology and reporting criteria--a 10-year update," *J. Vasc. Interv. Radiol.* **25**(11), 1691–705.e4 (2014).
50. S. J. Erickson-Bhatt, R. M. Nolan, N. D. Shemonski, S. G. Adie, J. Putney, D. Darga, D. T. McCormick, A. J. Cittadine, A. M. Zysk, M. Marjanovic, E. J. Chaney, G. L. Monroy, F. A. South, K. A. Craddock, Z. G. Liu, M. Sundaram, P. S. Ray, and S. A. Boppart, "Real-time imaging of the resection bed using a handheld probe to reduce incidence of microscopic positive margins in cancer surgery," *Cancer Res.* **75**(18), 3706–3712 (2015).
51. W.-C. Kuo, J. Kim, N. D. Shemonski, E. J. Chaney, D. R. Spillman, Jr., and S. A. Boppart, "Real-time three-dimensional optical coherence tomography image-guided core-needle biopsy system," *Biomed. Opt. Express* **3**(6), 1149–1161 (2012).
52. P.-C. Huang, P. Pande, R. L. Shelton, F. Joa, D. Moore, E. Gillman, K. Kidd, R. M. Nolan, M. Odio, A. Carr, and S. A. Boppart, "Quantitative characterization of mechanically indented *in vivo* human skin in adults and infants using optical coherence tomography," *J. Biomed. Opt.* **22**(3), 34001 (2017).